RSC Advances

ROYAL SOCIETY OF CHEMISTRY

PAPER

View Article Online
View Journal | View Issue

Cite this: *RSC Adv.*, 2026, **16**, 7163

Sol–gel derived silica-based 58S bioactive glass as a carrier for *Andrographis paniculata* extract in antibacterial dental applications

Ngoc-Dung Huynh Luu, [ab] Thi-Phuong Nguyen[c] and Thi-Le-Hang Dang *[d]

Dental caries and associated oral infections require biomaterials that promote remineralization while controlling bacterial growth and maintaining cytocompatibility. In this study, a sol–gel-derived silica-based 58S bioactive glass was investigated as a carrier for *Andrographis paniculata* (AP) extract (AP@58S-2) for antibacterial dental applications. Spherical 58S particles were synthesized *via* a two-step sol–gel route, yielding an amorphous glass with a high specific surface area of 786.3 m^2 g^{-1} and mesopores distributed in the 1.49–2.14 nm range, as confirmed by SEM, TEM, XRD, and nitrogen adsorption analyses. Compared with glass prepared by a one-step method, the two-step 58S exhibited a more uniform morphology and moderate pH variation during immersion, which is favorable for cellular compatibility. The mesoporous structure enabled efficient AP extract loading (~65%, corresponding to ~10.6 μg extract per mg glass) and supported sustained release of andrographolide, reaching approximately 70% cumulative release within 24 h under simulated physiological conditions. *In vitro* cytocompatibility assays demonstrated that AP@58S-2 maintained hMSC viability above 90% across the tested extract concentrations. Antibacterial evaluation against *Streptococcus mutans* revealed enhanced efficacy for AP@58S-2 compared with the unloaded bioactive glass, with a minimum inhibitory concentration of 1.5 mg mL^{-1} and bactericidal behavior indicated by an MBC/MIC ratio of 1.33, together with a time-dependent reduction in biofilm viability. AP@58S-2 demonstrated potent antioxidant activity through effective DPPH and ABTS radical scavenging and significantly reduced nitric oxide generation in LPS-stimulated RAW 264.7 cells. These results indicate that morphology-controlled 58S bioactive glass can function as an effective carrier for plant-derived bioactive compounds, providing combined mineralization-related bioactivity, antibacterial effects, and antioxidant functionality. This integrated approach is relevant for dental applications where infection control and oxidative stress management are required alongside tissue regeneration.

Received 13th August 2025
Accepted 24th January 2026

DOI: 10.1039/d5ra05958e

rsc.li/rsc-advances

1. Introduction

Dental caries and associated oral infections remain among the most prevalent health problems worldwide, affecting populations across all age groups.[1,2] The pathogenesis of tooth decay involves a complex interplay between demineralization of hard tissues and the proliferation of cariogenic bacteria, most notably *Streptococcus mutans*.[3] Effective management requires not only the restoration of mineral content but also the suppression of microbial colonization and the control of local inflammation.[2] Conventional restorative materials often address only one aspect of the problem—either providing structural replacement or delivering antibacterial agents—but rarely achieve long-term, multifunctional protection and regeneration.[3] This gap has driven the search for advanced biomaterials that can simultaneously promote remineralization, inhibit bacterial growth, and support tissue healing.[2,4]

Bioactive glasses (BGs) are considered promising materials because of their inherent remineralization ability and pH-mediated antibacterial effects.[4] First developed for bone regeneration, BGs are silica-based materials capable of forming a direct bond with hard tissues through the formation of a hydroxycarbonate apatite (HCA) layer on their surface.[5,6] This bioactive reaction is particularly valuable in dentistry, as it mimics the natural mineral phase of enamel and dentin.[4] Among the various compositions, 58S bioactive glass—comprising 60 mol% SiO_2, 36 mol% CaO, and 4 mol% P_2O_5—has been extensively studied for its high calcium oxide content and optimized Ca/P ratio, which together enhance mineral

[a]*Department of Pharmacology – Clinical Pharmacy, Faculty of Pharmacy, University of Health Sciences, Ho Chi Minh City, 700000, Viet Nam. E-mail: lhndung@uhsvnu.edu.vn*

[b]*Vietnam National University Ho Chi Minh City, Ho Chi Minh City, 700000, Viet Nam*

[c]*Faculty of chemical technology, Ho Chi Minh City University of industry and trade, Ho Chi Minh City, 700000, Viet Nam*

[d]*Institute of Advanced Technology, Vietnam Academy of Science and Technology, Ho Chi Minh, 70000, Viet Nam. E-mail: dtlhang@iat.vast.vn*

deposition and biological performance.[5,7] When in contact with saliva or physiological fluids, 58S rapidly releases calcium and phosphate ions from its network, triggering the nucleation of HCA and stimulating osteoblast activity, which is critical for periodontal and periapical bone regeneration.[8] In addition to its mineralizing capability, the high calcium content of 58S creates a locally alkaline environment during dissolution, which is inhospitable to many oral pathogens, imparting it with an intrinsic antibacterial effect.[4] Furthermore, 58S exhibits excellent biocompatibility and chemical stability, and its composition can be tailored for specific clinical needs, making it an attractive platform for oral applications.[7,8] However, its performance is strongly influenced by particle morphology.[9] Numerous studies have shown that spherical BG particles possess superior properties compared to irregular ones.[9,10] Spherical particles offer a larger surface area, more uniform porosity, and higher densities of surface hydroxyl groups, all of which increase ion exchange rates and bioactivity.[10] These structural advantages also enhance osteogenic potential, making spherical BGs highly desirable for dental regeneration.[9]

Achieving uniform spherical morphology, however, can be challenging with conventional one-step sol–gel synthesis, which often produces irregularly shaped and aggregated particles. The two-step sol–gel method offers a straightforward and practical approach to overcome this limitation.[11,12] In the first step, silica nanoparticles are formed and purified to ensure controlled particle growth and shape. In the second step, calcium and phosphate are incorporated in a controlled manner, minimizing structural disruption. This method yields monodisperse spherical particles with high surface area and open mesopores.[11] Such well-defined morphology not only enhances bioactivity but also enables controlled ion release, thereby moderating the pH rise during immersion.[13] This is especially important in the oral cavity, where excessive alkalinity can damage surrounding soft tissues and impair cell viability.

While morphology improves the baseline performance of 58S, its functional range can be further expanded by incorporating bioactive agents with antimicrobial and antioxidant properties.[1,14] *Andrographis paniculata* (AP) is a medicinal plant widely used in traditional Asian medicine, rich in phenolic and flavonoid compounds, as well as the diterpenoid lactone andrographolide.[15,16] These phytochemicals exhibit strong antibacterial, anti-inflammatory, and antioxidant activities, making AP a promising candidate for oral health applications.[16] Karumaran *et al.* demonstrated that AP extract supports the osteogenic and odontogenic differentiation of human dental pulp stem cells.[16] Plianrungsi *et al.*[17] reported the use of AP extract as an adjunct in chronic periodontitis treatment due to its antioxidant effects. Muhamad Alojid *et al.*[18] showed potent antibacterial activity of AP extract against *P. gingivalis*, *S. mutans*, and *S. sobrinus*. Therefore, the combination of 58S bioactive glass and AP extract would offer a synergistic strategy for dental and oral tissue engineering. The bioactive glass provides a structural and mineralizing scaffold with inherent antibacterial alkalinity, while the AP extract delivers plant-derived compounds that can actively suppress bacterial growth, reduce oxidative stress, and modulate inflammation. In the specific case of *S. mutans*, this dual approach could both disrupt biofilm formation and promote remineralization of early carious lesions. Moreover, the mesoporous structure of spherical 58S provides an ideal reservoir for AP loading, enabling controlled release of its bioactive constituents directly at the site of need.

2In this study, we developed a spherical 58S bioactive glass integrated with AP extract (AP@58S-2) for targeted antibacterial dental application, specifically aimed at the prevention and management of tooth decay. The 58S glass was synthesized *via* the two-step sol–gel route to ensure spherical morphology, high surface area, and open mesoporosity for AP loading and pH regulation. The AP@58S-2 was evaluated for its structural characteristics, bioactivity, andrographolide release kinetics, cytocompatibility with human mesenchymal stem cells (hMSCs), antioxidant potential, and antibacterial activity against *S. mutans*. This work integrates particle morphology control, pH moderation, and targeted to bioactive delivery into a single multifunctional material platform, addressing the combined needs of remineralization, infection control, and oxidative stress management in oral and dental regenerative therapies.

2. Materials and methods

2.1 Materials

Tetraethyl orthosilicate (TEOS, ≥98%), triethyl phosphate (TEP, 99%), calcium nitrate tetrahydrate ($Ca(NO_3)_2 \cdot 4H_2O$, ≥99%), ammonium hydroxide (28–30 wt%), and hexadecyltrimethylammonium bromide (CTAB, ≥99%) were purchased from Acros Organics (USA). 2,2-Diphenyl-1-picrylhydrazyl (DPPH) and ABTS reagents were obtained from Mackun (China). Andrographolide standard, propidium iodide (PI), and lipopolysaccharides (LPS) from *Escherichia coli* O111:B4, Griess reagent were purchased from Sigma-Aldrich (USA). Cell culture reagents—Minimum Essential Medium (MEM), fetal bovine serum (FBS), penicillin–streptomycin, sodium bicarbonate, trypsin–EDTA, and phosphate-buffered saline (PBS, 1×)—were supplied by Gibco. Acridine orange (AO) was obtained from Alfa Aesar, and Hoechst 33342 was supplied by Thermo Scientific. The SRB cell proliferation kit (ab235935) was purchased from Abcam. All organic solvents used for synthesis and characterization were HPLC grade and obtained from Fisher Chemical. Absolute ethanol was supplied by VN-CHEMSOL (Viet Nam). *Andrographis paniculata* plant material (dried leaf) was purchased from Tue Tam Herbal Company Limited (Viet Nam). Human mesenchymal stem cells (hMSCs, 4th passage) were obtained from Loza Biotech, Mouse Monocyte-Macrophage Leukemia Cells (Raw 264.7, 5th passage) were come from American Type Culture Collection ATCC (USA); and *Streptococcus mutans* (*S. mutans*) was kindly provided by Dr Tuan Tran (University of Science, Vietnam National University, Ho Chi Minh City).

2.2 Preparation of bioactive glass

Bioactive glass with the nominal composition 58S (60 mol% SiO_2, 36 mol% CaO, 4 mol% P_2O_5) was synthesized using two

distinct sol–gel approaches: a conventional one-step method (58S-1) and a modified two-step sol–gel method (58S-2) developed in this work.

2.2.1 One-step sol–gel method (58S-1). CTAB (0.5 g) was dissolved in ethanol (100 mL), followed by the addition of ammonium hydroxide 25 w/w% (5 mL). 4.48 mL of tetraethyl orthosilicate (TEOS) was then added to the mixture, followed by 0.454 mL of triethyl phosphate (TEP). After 24 h of stirring at room temperature, calcium nitrate tetrahydrate (CaNT, 2.83 g) was introduced, and the reaction was continued for an additional 24 h. The resulting colloidal suspension was collected by centrifugation at 5000 rpm for 15 min. The precipitate was washed sequentially with ethanol and deionized water, filtered under vacuum, and dried at 70 °C overnight. The dried powder was calcined at 700 °C for 5 h using a heating rate of 2 °C min^{-1}.

2.2.2 Modified two-step sol–gel method (58S-2). CTAB (0.5 g) was first dissolved in 100 mL ethanol, followed by the addition of ammonium hydroxide 25 w/w% (5 mL). 4.48 mL of TEOS was then introduced, and 0.454 mL of TEP was added after 2 h. The reaction mixture was stirred at 60 °C for 3 h. The colloidal suspension was collected by centrifugation at 5000 rpm for 15 min, and the precipitate was washed sequentially with ethanol and deionized water before filtration under vacuum. Unlike method 2.2.1, the obtained powder was dried and subsequently re-dispersed in 100 mL of ethanol, after which 2.83 g of CaNT was added and the mixture was stirred for 24 h. The product was collected by centrifugation, washed sequentially with ethanol and deionized water, and filtered under vacuum. The final white powder was dried at 70 °C overnight and calcined at 700 °C for 5 h with a heating rate of 2 °C min^{-1}.

2.3 Characterization of bioactive glass

2.3.1 Morphology, pore structure and crystal structure. The synthesized bioactive glasses were characterized using scanning electron microscopy (SEM, Jeol, Japan) equipped with energy-dispersive spectroscopy (EDS), transmission electron microscope (TEM, JEM-2100, Jeol, Japan), X-ray diffraction (XRD, BRUKER D8 Advance), Brunauer–Emmett–Teller (BET, Quantachrome Nova 2000e) surface area analysis.

2.3.2 Calcium ion release and pH variation. To evaluate the *in vitro* bioactivity of the synthesized bioactive glasses (BGs), calcium ion release was investigated under physiological-like conditions. Briefly, 100 mg of BG powder was immersed in 50 mL of Dulbecco's Modified Eagle Medium (DMEM, Gibco) and incubated at 37 °C in an orbital shaker to ensure homogeneous dispersion. At predetermined time intervals, aliquots of the immersion medium were withdrawn and analyzed for calcium ion concentration using inductively coupled plasma-optical emission spectroscopy (ICP-OES, Horiba). Simultaneously, the pH of the immersion medium was recorded at each time point using a calibrated digital pH meter (Mettler Toledo). Monitoring both Ca^{2+} release and pH variation provides insight into glass dissolution behavior and ionic exchange processes, which are critical indicators of bioactivity.

2.3.3 *In vitro* biomineralization in simulated body fluid. The biomineralization ability of the BGs was assessed by immersion in simulated body fluid (SBF) at pH 7.4, following established *in vitro* bioactivity protocols. The samples were incubated at 37 °C under static conditions to mimic physiological temperature. At designated time points, the samples were removed from SBF, and the precipitates formed on the glass surfaces were gently washed with deionized water to eliminate residual salts, followed by freeze-drying. The surface morphology of the mineralized layers was examined using SEM, while the crystalline phases of the formed apatite were identified by XRD.

2.4 Preparation of the crude extract

Dried leaves of *Andrographis paniculata* were soaked in 90% ethanol at a ratio of 1 g plant material to 10 mL solvent. The mixture was subjected to ultrasonic-assisted extraction for 5 h. The resulting suspension was filtered to remove solid residues, and the filtrate was concentrated under reduced pressure using a rotary evaporator. The concentrated extract was then dried under vacuum to obtain the ethanol-based *A. paniculata* extract.

The phytochemical screening for AP extract was done with total phenolic content and total flavonoid content, following the previous protocol.[19] The quantitative andrographolide was done by UV-vis at $\lambda_{max} = 227$ nm. A solution of andrographolide stock in ethanol was prepared at a concentration of 0.5 mg mL^{-1}. The standard concentration range for andrographolide was built from 0 to 0.05 mg mL^{-1} and was used to calculate the amount of andrographolide in the extract. The experiment was repeated at least 3 times.

2.5 Preparation of crude extract loaded bioactive glass

AP extract was dissolved in ethanol, 0.5 g/10 mL. Bioactive glass was added to this solution, and sonication was applied. AP-loaded bioactive glass was collected *via* a filter vacuum. Ethanol was used to wash the product, and the free-drying was applied to collect the product. The product was analyzed by TEM and BET. The loading efficacy and the release study were determined *via* the concentration of andrographolide.

2.6 The *in vitro* cell test

The cytotoxicity of the bioactive glass powders was evaluated using human mesenchymal stem cells (hMSCs). BG powder was dispersed in DMEM at a concentration of 10 mg mL^{-1}. The suspension was incubated at 37 °C for 24 h under gentle agitation to obtain the material extract. After incubation, the extract solution was collected and filtered to remove particulate matter. The resulting extract was subsequently diluted with fresh culture medium to final concentrations of 50% and 10% for cytotoxicity evaluation. After the designated incubation period, cell viability was evaluated using the sulforhodamine B (SRB) assay (SRB Assay Kit, ab235935, Abcam), according to the protocol of the manufacturer. For qualitative assessment of cell viability, triple fluorescence staining with acridine orange (AO), propidium iodide (PI), and Hoechst 33342 was performed to visualize live and dead cells under a fluorescence microscope. AO stained viable cells green, PI stained membrane-compromised (dead) cells red, and Hoechst 33342 stained cell nuclei blue.

2.7 Anti-oxidation assay

The antioxidant property of products was determined *via* DPPH assay, ATBS assay, and nitric oxide. The procedure for DPPH, ATBS, and nitric oxide was followed from the previous study.[19]

2.8 Anti-bacterial activity

The samples were dispersed in distilled water with the aid of ultrasonication. The minimum inhibitory concentration (MIC) and minimal bactericidal concentration (MBC) against *Streptococcus mutans* were determined using the microdilution method. A bacterial suspension of *S. mutans* (1.0×10^7 CFU mL^{-1}) was prepared in Brain Heart Infusion (BHI, Himedia) broth. In a 96-well plate, 200 μL of bacterial suspension was added to each well, followed by 10 μL of the test sample at predetermined concentrations. Plates were incubated at 37 °C, and MIC and MBC values were recorded after 48 h. Chloramphenicol (20 μg mL^{-1}) served as the positive control, and distilled water was used as the negative control. For the zone of inhibition test, the antibacterial activity of each sample was further evaluated using the agar well diffusion method. Test disks impregnated with the samples were placed on BHI agar plates inoculated with *S. mutans*. After incubation at 37 °C for 18–24 h, the diameters of the inhibition zones (including the disk) were measured. Zone diameters ≤ 6 mm were considered inactive against the tested microorganism.

For the biofilm assay, *S. mutans was* cultured overnight in BHI medium supplemented with 2% sucrose (wt/vol). The inoculum (100 μL) was then transferred to a round-bottom 96 well plate. After 24 h of incubation, the adherent biofilms were refreshed with fresh medium and incubated for another 24 h. After that, AP@58S-2 (at MBC values) was added along with the fresh BHI medium. The plates were incubated statically at 37 °C for 24 h to allow biofilm formation in the presence of the materials. After incubation, planktonic bacteria were carefully removed, and the wells were gently washed three times with sterile phosphate-buffered saline to eliminate non-adherent cells. The remaining biofilms were air-dried and stained with 0.1% (w/v) crystal violet solution for 15 min at room temperature. Excess stain was removed by thorough washing with deionized water, and the bound crystal violet was solubilized using ethanol. The absorbance was measured at 570 nm using a microplate reader to quantify biofilm biomass. All experiments were performed in triplicate.

2.9 Statistical test

All the data were presented as mean ± SD (n at least 3). The Shapiro–Wilk normality test evaluated data collected from cell culture and microbial viability assessment. All the data was collected using Origin 2024b.

3. Results and discussion

3.1 Structural and morphological characterization of 58S bioactive glass nanoparticles

3.1.1 Particle morphology. The particle morphology of sol–gel-derived 58S glass was studied as a function of processing steps using SEM, TEM, and EDS analyses. Particles were synthesized following two main protocols: a one-step method

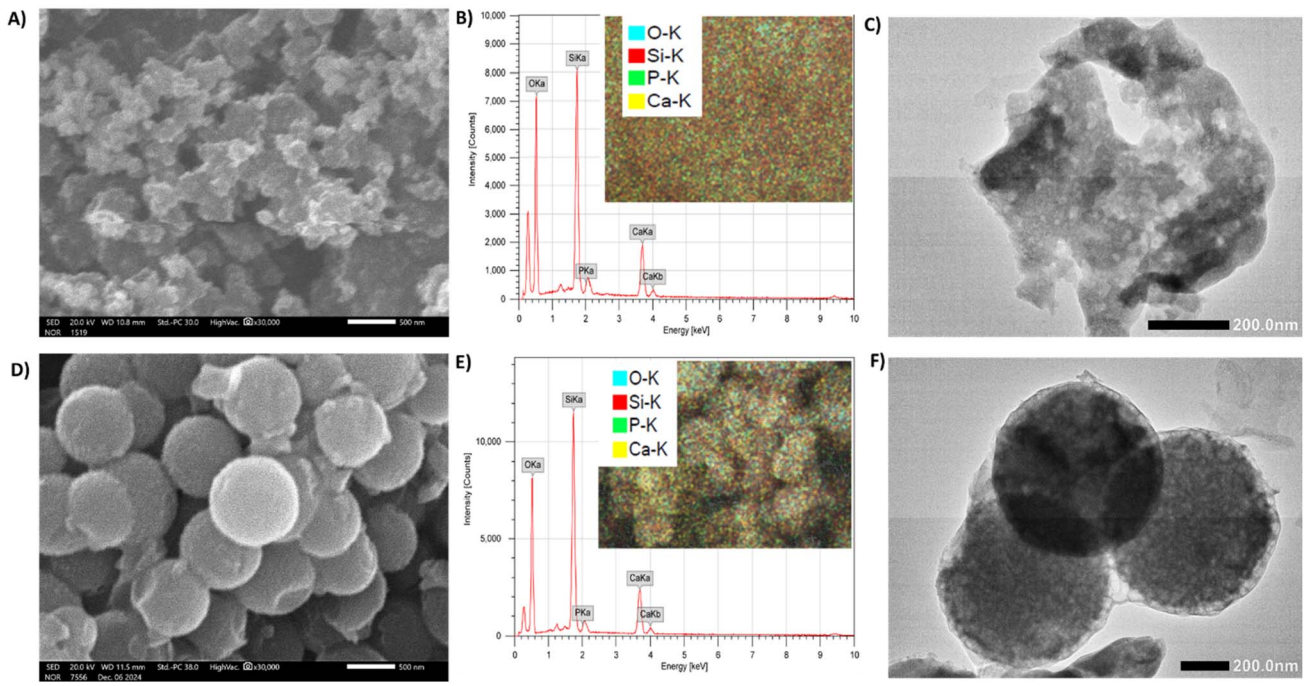

Fig. 1 Morphological and compositional characterization of samples prepared by the one-step (58S-1) and two-step (58S-2) synthesis methods. (A) SEM micrograph, (B) EDX spectrum with corresponding elemental mapping, and (C) TEM image of 58S-1. (D) SEM micrograph, (E) EDX spectrum with corresponding elemental mapping, and (F) TEM image of 58S-2.

(58S-1) and a two-step method (58S-2). As shown in Fig. 1, the two types of 58S glass exhibited significantly different morphologies, despite nearly identical compositions. The SEM images revealed that 58S-1 particles exhibited an irregular morphology with pronounced aggregation. This behavior can be attributed to the role of CTAB in the sol–gel process, where it acts as a soft template or nanoreactor; variations in droplet fusion and deformation during hydrolysis and condensation can result in non-uniform particle growth.[9,10,13] The introduction of metal ions destabilizes the nanoparticles by affecting the condensation of TEOS, thereby altering their morphology.[12] It had been reported that the addition of CaNT induced a substantial impact on bioactive glass morphology,[20] which is consistent with the aggregated structure observed for 58S-1. To further elucidate the effect of calcium addition timing, another 58S-1 was prepared, namely 58S-1-2 h and 58S-1-24 h. In this way, the CaNT was added to the reaction after 2 h and 24 h of TEOS–TEP hydrolysis. Both 58S-1-2 h and 58S-1-24 h were spherical, but the amount of CaO was lower than 10 mol%, lower than that of the nominal composition and 58S, in agreement with previous reports.[20] In a typical Stöber process, silica nanoparticles form within seconds or minutes after the mixture of TEOS and the catalyst. The silica nanoparticle then continues to grow *via* Ostwald ripening, forming spherical secondary particles. These charged secondary particles can remain stable in particulate morphology without being bonded because they mutually repel each other under fundamental conditions. However, the presence of Ca^{2+} ions may lead to the aggregation of silica particles due to electrostatic interactions between the hydrated silica surface and hydrated counterions, resulting in an uncontrolled morphology as in 58S-1.

In contrast, the two-step method yielded dense, spherical, and monodispersed particles with a diameter of around ~400 nm were achieved. TEM analysis provided additional insight into the internal structure of these particles. TEM images of 58S-1 confirmed the presence of irregular, loosely packed aggregates with non-uniform contrast, indicating structural heterogeneity at the nanoscale. Meanwhile, 58S-2 particles exhibited well-defined spherical morphology with more homogeneous internal contrast, suggesting a denser and more uniform structure. This supports the notion that separating silica particle formation from calcium incorporation allows better control over particle growth and internal organization.

As mentioned above, silica nanoparticles form quickly and subsequently grow by Ostwald ripening under strongly basic conditions. The removal of these excess unreacted precursors is necessary, since excess TEOS and ammonium may cause further undesired reactions during the drying process, and excess calcium nitrates in sols may form calcium hydroxide instead of being incorporated into the silica particles.[13] By the separation process, silica nanoparticles were formed first. Then, Ca^{2+} ions can be adsorbed onto the surface of silica particles due to the electrostatic interactions between the positively charged Ca^{2+} ions and the negatively charged Si–OH groups. They could also form hydrated calcium silicate with $[SiO_4]^{4-}$ groups and (or) calcium hydroxide with OH^- groups. SEM-EDS elemental mapping and spectra indicated that both 58S-1 and 58S-2 exhibited comparable elemental compositions, confirming that both synthesis routes are effective in incorporating the constituent elements. However, the combined SEM and TEM results clearly demonstrate that the two-step method offers

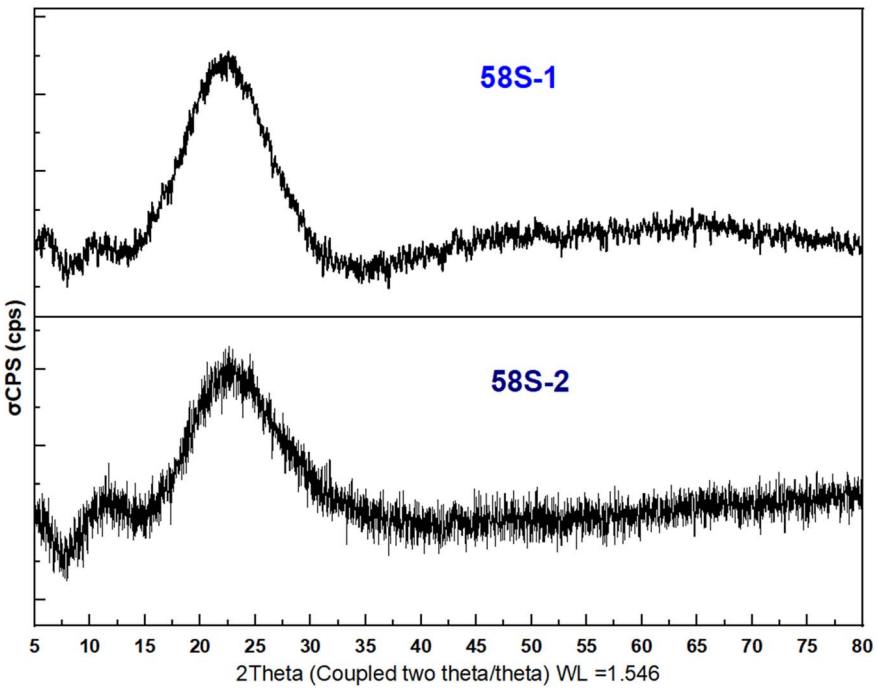

Fig. 2 XRD pattern of BG58S powder synthesized with one-step and two-step methods.

superior control over particle morphology and internal structure, despite similar overall chemical compositions.

3.1.2 X-ray diffraction analysis of glass structure. The effect of the processing method on the crystal structure of BG 58S was assessed by XRD. As shown in Fig. 2, the X-ray diffraction patterns obtained for 58S-1 and 58S-2 glasses exhibit broad signals in the ranges $2\theta = 12–31°$ and $2\theta = 12–30°$, respectively, which suggests the amorphous nature of the bioactive glass sample. The disordered structure of glass confers unique bioactive and physicochemical properties, enabling the fine-tuning of ionic species with biological significance.[11] The maximum of the amorphous halo observed in the XRD pattern for the bioactive glass 58S-1 is $2\theta = 22°$, which is similar to that observed for the 58S-2 glass. This confirmed the similarity in the distribution of distances relative to a reference $[SiO_4]$ tetrahedron, which is reflected in the number of atoms of the second nearest neighbor.

3.1.3 Porosity evaluation. The pore characteristics of the nanoparticles were further evaluated using nitrogen adsorption/desorption analysis, as shown in Fig. 3. Both 58S-1 and 58S-2 bioactive glasses exhibited type-IV isotherms, characteristic of open mesoporous structures.[13] The Brunauer–Emmett–Teller (BET) specific surface area, calculated from the linear portion of the BET plot, was 166.10 $m^2\ g^{-1}$ for 58S-1, which is more than four times smaller than the value obtained for 58S-2 (786.34 $m^2\ g^{-1}$). The micropore volume increased from 0.059 $cm^3\ g^{-1}$ in 58S-1 to 0.279 $cm^3\ g^{-1}$ in 58S-2, correlating with the significantly higher surface area of the latter. Hysteresis loop analysis further revealed differences in mesopore architecture between the two samples, consistent with the spherical morphology and homogeneous internal contrast observed in TEM (Fig. 1C and E). For 58S-1, the hysteresis loop appeared at a high relative pressure (0.8–1.0P/P_0), suggesting capillary condensation in larger, less interconnected mesopores. This behavior is characteristic of an ink-bottle type pore structure, where wide cavities are connected by narrow necks, potentially leading to pore blockage and reduced mass transport.[21] By comparison, 58S-2 exhibited a hysteresis loop over a broader relative pressure range (0.5–1.0P/P_0), indicative of a more open and interconnected mesoporous system. The presence of well-ordered mesopore networks with open-ended tubular channels suggests improved pore accessibility and mechanical integrity of the particles. This hierarchical pore architecture, together with the significantly higher surface area and pore volume, renders 58S-2 a more suitable

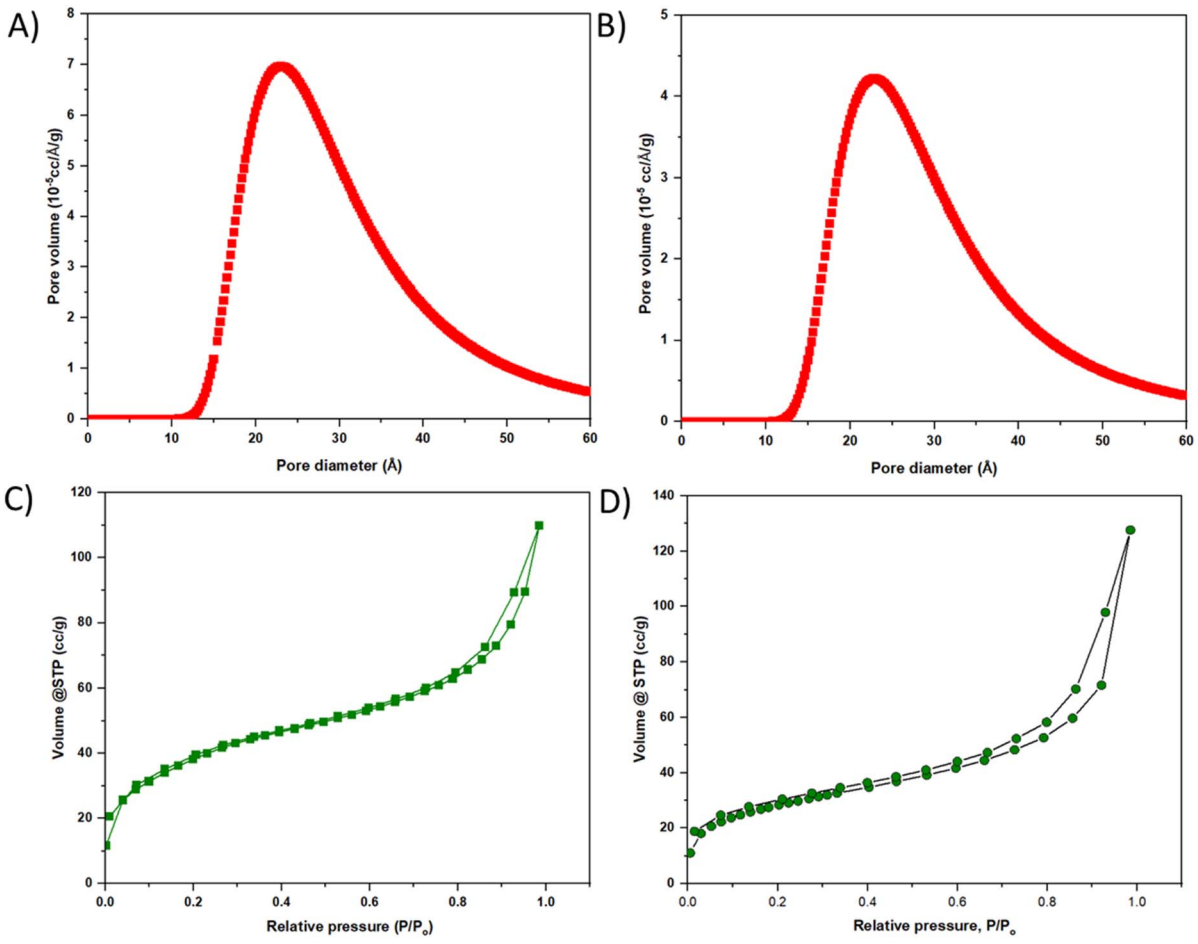

Fig. 3 BET graphs of the 58S powder in terms of pore volume (10^{-5} cm^3 $Å^{-1}$ g^{-1}) *versus* pore diameter (Å): (A) 58S-1, (B) 58S-2, and the nitrogen absorbed *versus* relative pressure P/P_0: (C) 58S-1, (D) 58S-2.

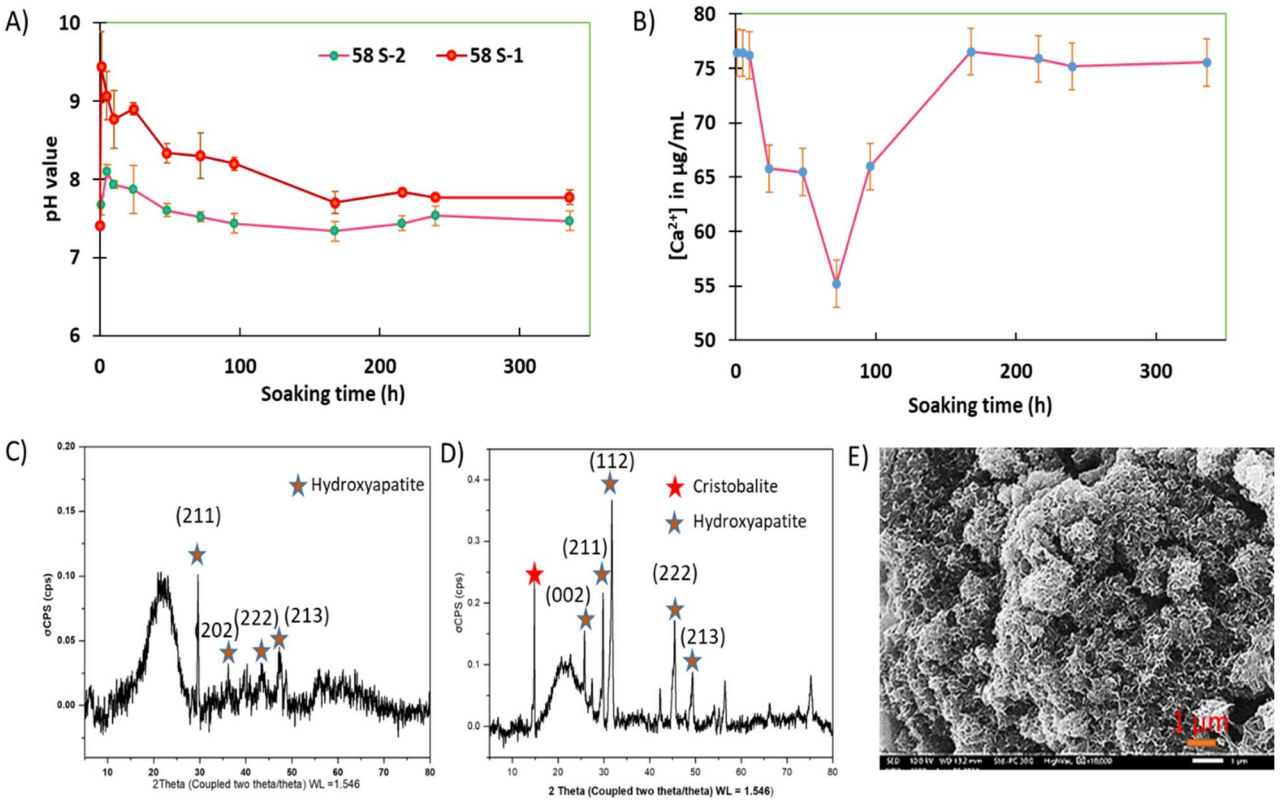

Fig. 4 (A) Evolution of pH and (B) variation of Ca^{2+} concentration in DMEM as a function of soaking time. Data were presented as mean ± SD ($n = 5$). XRD pattern of 58S-2 after (C) 14 days of SBF immersion and (D) after 28 days of immersion. (E) SEM micrograph of the 58S-2 after 28 days of SBF immersion, magnification 10000×.

candidate for drug delivery applications, as it enables efficient drug loading and controlled release of therapeutic molecules.[9]

3.2 Ion release behavior and pH evolution dynamics

Next, the change in localized pH resulting from the ion exchange reactions of the two types of 58S bioactive glass was evaluated. As shown in Fig. 4A, upon immersion, the pH rose rapidly within the first hour, indicating the immediate exchange of protons in the medium with cations (primarily Ca^{2+}) released from the glass surface. The pH reached its peak within the first few hours and then gradually declined, approaching a near-stable value after 168 h, reflecting the balance between ion release and hydroxycarbonate apatite (HCA) precipitation. Notably, 58S-1 exhibited a pronounced pH change due to a high rate of ion exchange, leading to a burst release of ions upon contact with the cell culture medium. In contrast, 58S-2 clearly limited the extent of pH excursion. While an alkaline environment generated by bioactive glass is essential for initiating HCA formation, an excessively rapid pH increase can negatively affect cell metabolism and function.[9] The two-step preparation method used for 58S-2 allows excess ions to be washed out, thereby preventing a rapid and drastic pH fluctuation.[13] In light of these insights, our work demonstrates that the separation route in synthesis 58S glass yields a hierarchically structured material endowed with higher levels of porosity and textural properties.

The bioactive properties of the bioactive glass were identified *via* the precipitation of calcium, leading to the formation of HCA on the glass surface. In this study, the mimetic cell culture environment, DMEM, with the concentration of Ca^{2+} at 72.1 µg mL^{-1}, was used to evaluate the activity of BG. The Ca^{2+} was 76.44 µg mL^{-1} after the first hour of soaking due to the ion exchange from the glass network with H^+ ions in the medium, leading to the accumulation of calcium ions in the medium, which was responsible for the formation of the strongly alkaline environment. Notably, the concentration of Ca^{2+} was reduced to 55.177 µg mL^{-1} following 72 days of immersion (Fig. 4B). The slightly decreased pH value of the medium was supported by a prominent ion exchange reaction leading to the formation of hydroxycarbonate apatite on the surface, consuming OH^- and phosphate from solution.[22] After this depletion phase, calcium levels recovered slightly and stabilized between 168 and 336 h, indicating reduced glass dissolution and dynamic equilibrium between release and precipitation processes.

3.3 *In vitro* bioactivity and biomineralization behavior

X-ray diffraction analysis confirmed the time-dependent structural evolution of the 58S-2 bioactive glass upon immersion in SBF. The as-prepared sample exhibited a broad diffraction halo in the range of 20–35° (2θ), which is characteristic of an amorphous silicate network (Fig. 2). After 7 days of immersion, the diffraction pattern remained largely dominated by the

amorphous halo; however, weak and broad diffraction features began to emerge, suggesting the initial formation of a poorly ordered calcium phosphate phase on the glass surface (Fig. 4C). These features indicate the early stages of surface mineralization with the diffraction features associated with HCA appeared, notably at the (211), (202), (222) and (213) plane. After 28 days of immersion, several diffraction peaks became more discernible, reflecting a gradual structural reorganization of the surface layer with prolonged soaking time (Fig. 4D). In particular, the appearance of a low-angle diffraction feature at approximately 15–16° (2θ) is attributed to the partial crystallization or structural rearrangement of the silica-rich surface layer and the formation of secondary crystalline phases, highlighting the time-dependent nature of the bioactivity process. SEM revealed that after 28 days of SBF immersion, the glass surface was uniformly covered by a continuous, nanoscale, cauliflower-like layer (Fig. 4E), which is a morphological hallmark of bone-like apatite formed under biomimetic conditions. This surface morphology is consistent with the progressive mineralization inferred from the XRD results. Taken together, the evolution of pH and Ca^{2+} concentration in solution, along with the structural and morphological analyses, demonstrates the high bioactivity of the 58S glass, characterized by the gradual nucleation and growth of a biologically relevant apatite-like layer under simulated physiological conditions.

3.4 Phytochemical profile and loading behavior

3.4.1 Phytochemical characterization of *Andrographis paniculata* extract. The ethanol extract of AP demonstrated notable phytochemical richness and bioactivity. Phytochemical screening revealed a high total phenolic content (187.6 ± 1.22 mg GAE per g), indicating strong antioxidant potential, along with a total flavonoid content of 57.2 ± 2.55 mg QE per g. Andrographolide, a characteristic diterpenoid lactone and key bioactive marker of AP, was quantified at 5.72 ± 0.11 mg g^{-1} by UV-vis analysis. Biological assays supported these findings: the extract exhibited moderate antioxidant activity with IC_{50} values of 287.14 ± 10.14 μg per mL (DPPH) and 215.12 ± 4.22 μg per mL (ABTS), consistent with phenolic-driven free radical scavenging. Antibacterial evaluation revealed marked inhibitory effects against *S. mutans*, with a minimum inhibitory concentration (MIC) of 0.25 mg mL^{-1}, suggesting potential applications in oral health. Overall, these results highlight the extract with the rich phytochemical profile and functional bioactivities, particularly its antioxidant and antibacterial properties (Table 1).

3.4.2 *Andrographis paniculata* extract loading bioactive glass. The loading of AP extract into the bioactive glass 58S-2 (AP@S58-2) was achieved through a post-synthesis adsorption (impregnation) method (Fig. 5A), which takes advantage of the high specific surface area and interconnected mesoporous structure of the glass.[23–25] The morphology of AP@S58-2 (Fig. 5B) was identical to that of the bare S58-2 (Fig. 1F), confirming that loading processes did not affect the morphology of the glass particles. However, the mesopores of AP@S58-2 seem to be closed. In addition, the dramatic decrease in micropore volume (from 0.279 to 0.005 cm^3 g^{-1}) observed in the BET results, confirming that the pores were filled with AP extract. The amount of AP extract loaded into 58S-2 was measured by UV-vis spectroscopy based on the absorption of andrographolide. About 65% AP was loaded into S58-2, accounting for 10.6 μg AP per mg 58S-2.

One of the greatest challenges of conventional drug delivery systems is the administration of multiple doses in a short time due to the high concentration fluctuation in the blood. One strategy to combat this challenge is using specific drug nanocarriers, which could ensure prolonged drug release.[26] Hence, *in vitro* release studies were carried out to investigate the potential of 58S-2 in carrying AP extract. It could be seen from Fig. 5C that the andrographolide release rate was fast in the first 10 h, and gradually became flat after 10 h. The initial burst release indicates that AP extract molecules that were adhered onto the surface of the 58S-2 diffused out rapidly into the solution. After that, a controlled release of extract from 58S-2 was measured. The reason for the controlled release might be that most of the AP molecules adsorbed onto the surface of the 58 *via* electrostatic interactions or were accumulated in the mesoporous channels.[27] The cumulative release from AP@58S-2 reached 70% of the total loading after 24 h. This 58S-2 could achieve short-term stable drug release, so it had good application potential for oral dental disease.

3.5 Antibacterial and biological performance of AP-loaded 58S bioactive glass

3.5.1 *In vitro* cytotoxicity. A direct cytotoxicity assessment was performed in accordance with the ISO 10993-5 standard. In

Table 1 Ethanol *Andrographis paniculata* extract screening

Criteria	Term	Value
Phytochemical screening		
Total phenolic compound	mg GA per g	187.6 ± 1.22
Total flavonoid compound	mg QE per g	58.2 ± 2.55
Andrographolide	mg g^{-1}	5.72 ± 0.11
Biological functions screening		
DPPH assay	IC_{50}	287.14 ± 10.14 μg mL^{-1}
ABTS assay	IC_{50}	215.12 ± 4.22 μg mL^{-1}
Anti-bacteria: *Streptococcus mutans*	MIC	0.25 mg mL^{-1}
	MBC	0.75 mg mL^{-1}

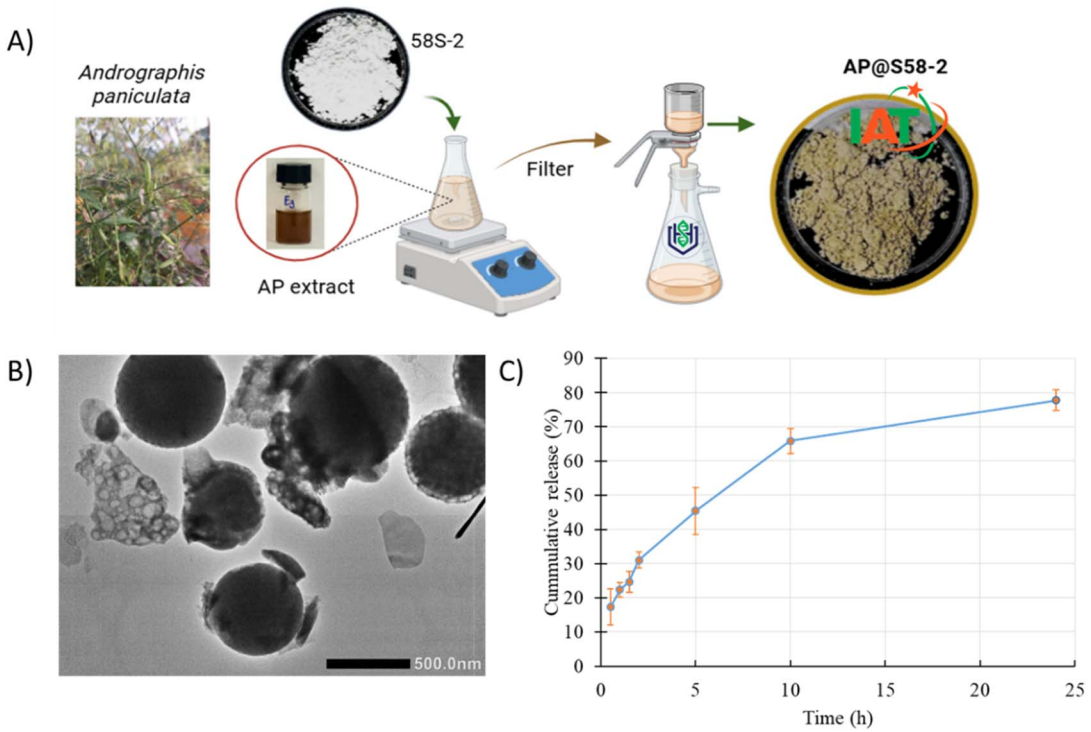

Fig. 5 (A) The synthesis route of AP@S58-2, (B) TEM image of AP@S58-2 and (C) the cumulative release of andrographolide from AP@S58-2 in SBF, 37 °C. Data was presented as mean ± SD ($n = 4$).

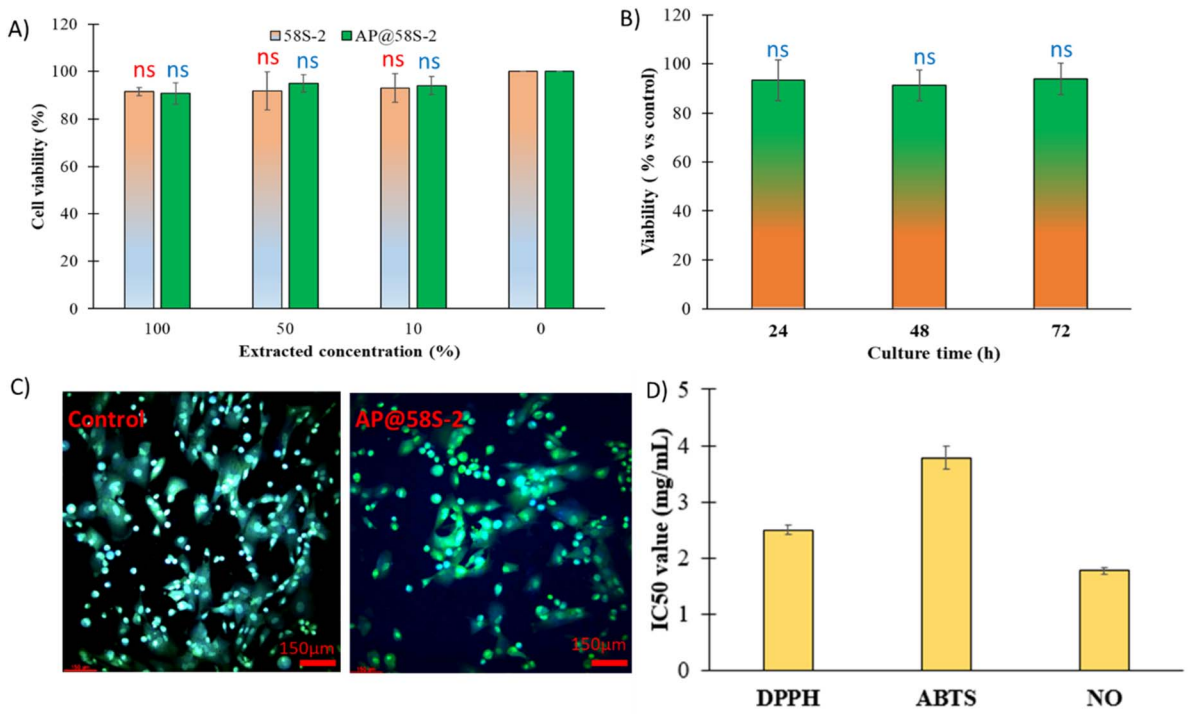

Fig. 6 (A) The cell viability of hMSCs cells after 24 h exposure to different extracted concentrations of the samples (58S-2 and AP@58S-2), ns (non-significant difference at $\alpha = 0.05$) compared with the control group; (B) the viability of hMSCs after difference time exposure to 100% extracted AP@58S-2, ns (non-significant difference at $\alpha = 0.05$) compared with the control group. Data was presented as mean ± SD ($n = 4$). (C) Live/dead analysis using Hoechst, acridine orange (AO), and propidium iodide (PI) on hMSC cells cultured with AP@58S-2 after 24 h, scale bar: 150 μm. (D) Antioxidant activity of the material evaluated by DPPH, ABTS, and nitric oxide (NO) radical scavenging assays, expressed as IC_{50} values (μg mL^{-1}).

this study, the cytotoxicity of AP@58S-2 and its as-prepared counterpart (58S-2) was evaluated by culturing human mesenchymal stem cells (hMSCs) with material extracts. The results are presented in Fig. 6A. Neither sample exhibited cytotoxic effects on hMSC viability, even at high extract concentrations. No statistically significant reduction in cell viability was observed across extract dilutions ranging from 100% (10 mg mL^{-1}) to 10%, compared with the control group (all $p > 0.1$). Cell proliferation was further assessed by monitoring the doubling time of hMSCs as a function of culture duration (Fig. 6B). The cellular response to AP@58S-2 at 10 mg mL^{-1} remained comparable to the control at all evaluated time points, with cell viability consistently exceeding 90% ($p > 0.1$). In addition, hMSCs cultured in the presence of AP@58S-2 were analyzed using combined Hoechst, acridine orange (AO), and propidium iodide (PI) staining (Fig. 6C). Hoechst staining revealed intact nuclei in both control and treated groups, indicating preserved nuclear integrity. Acridine orange staining showed a high density of viable, adherent cells emitting green fluorescence, while only a negligible number of PI-positive cells (red fluorescence) were detected, suggesting minimal membrane damage. These demonstrate that AP@58S-2 is well tolerated by hMSCs during the initial 24 h exposure period, with no evidence of acute cytotoxicity. The preservation of normal cell morphology and uniform cell distribution further indicates that the composite material and/or released ionic species do not adversely affect cell adhesion or viability, which is essential for subsequent regenerative medicine applications.

3.5.2 Antioxidant activity. Beyond biocompatibility, the antioxidant potential of AP@58S-2 was evaluated using three distinct radical scavenging assays—DPPH, ABTS, and nitric oxide—selected to probe different reactive species and scavenging mechanisms (Fig. 6D). IC_{50} values were calculated for each assay, where lower values indicate higher antioxidant activity. AP@58S-2 demonstrated broad and potent antioxidant activity across multiple assay systems. The sample exhibited effective free radical scavenging capacity, with half-maximal inhibitory concentrations (IC_{50}) of approximately 2.5 mg mL^{-1} and 3.78 mg mL^{-1} in the DPPH and ABTS radical scavenging assays, respectively. The pronounced radical scavenging ability suggests the presence of functional groups and bioactive phytochemicals, likely derived from the AP extract, capable of donating electrons or hydrogen atoms to neutralize radical species such as $DPPH^{\bullet}$ and $ABTS^{\bullet+}$. Furthermore, its antioxidant potential was corroborated through cellular-based evaluation. In an LPS-stimulated RAW 264.7 macrophage model, AP@58S-2 significantly suppressed nitric oxide (NO) production, achieving a 50% reduction at a concentration of 1.78 mg mL^{-1} when supplemented in the culture medium. This inhibitory effect indicates that AP@58S-2 may exert anti-inflammatory activity by

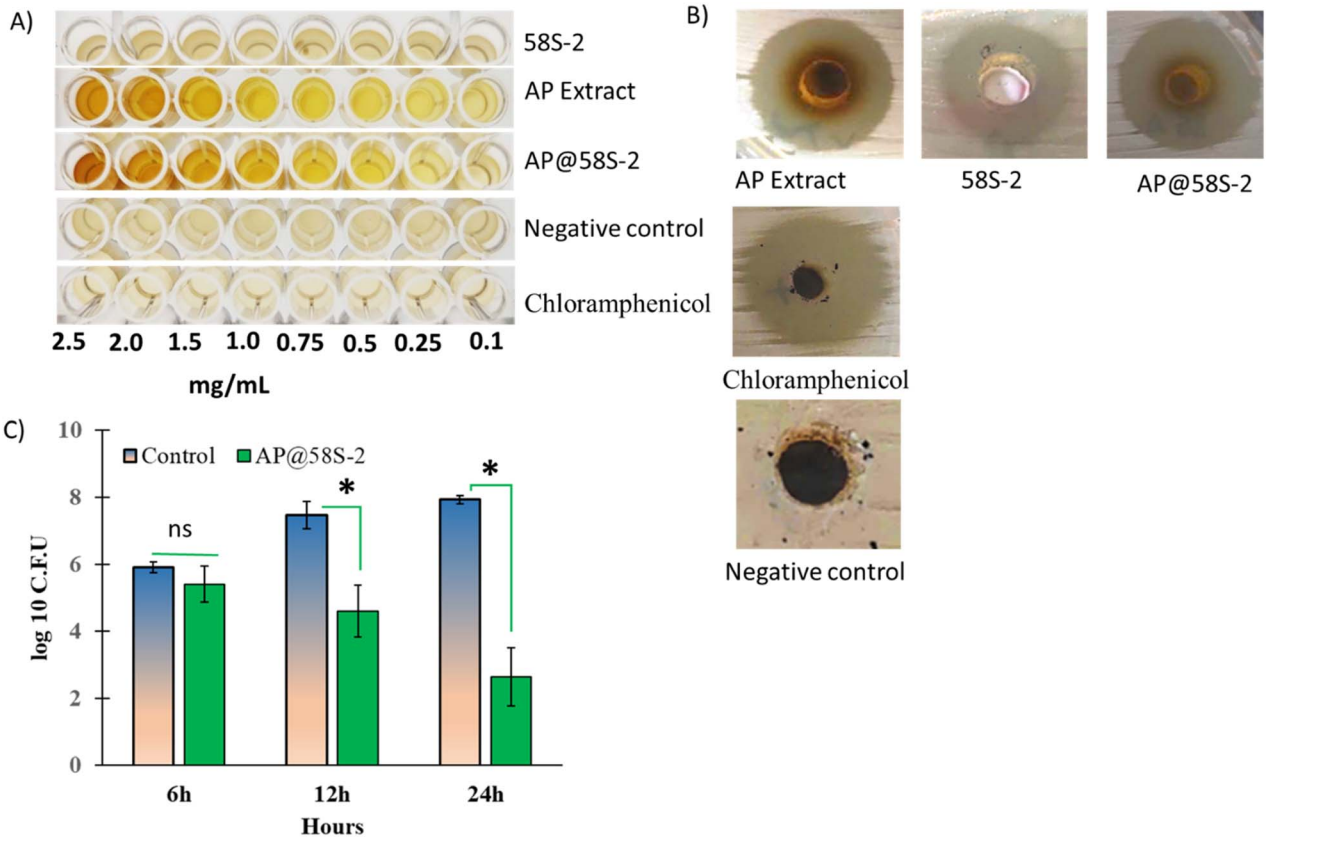

Fig. 7 Antibacterial activity of the 58S-based materials evaluated by complementary *in vitro* assays. (A) Representative photographs of a 96-well plate containing *S. mutans* exposed to various samples with varying concentration, (B) the zone inhibition at the MIC value of each tested samples, (C) the antibacterial performance of AP@58S-2 at 6, 12, and 24 h of incubation. Data was presented as mean ± SD ($n = 4$). Ns: non-significant difference at $\alpha = 0.05$ compared with the control group; * significant difference at $\alpha = 0.05$ compared with the control group.

modulating oxidative and nitrosative stress pathways in activated immune cells. Such properties are advantageous for biomedical implants or scaffolds, as oxidative stress is a common factor in tissue injury and chronic inflammation, and mitigating reactive oxygen and nitrogen species can help preserve cellular health and promote tissue regeneration.[1]

3.6 Anti-bacteria

The antibacterial potential of AP@58S-2 was examined against *Streptococcus mutans*, a cariogenic bacterium implicated in oral biofilm formation, to explore its suitability for applications in dental or oral tissue engineering.[14,18] In broth culture assays (Fig. 7A), bacterial growth was assessed at various concentrations of AP extract, 58S-2, and AP@58S-2 by visual inspection of turbidity. AP@58S-2 exhibited a concentration-dependent inhibition of bacterial growth, with increasing concentrations resulting in progressively clearer wells. The MIC values of the AP extract, 58S-2, and AP@58S-2 were 0.25 mg mL^{-1}, 2.5 mg mL^{-1}, and 1.5 mg mL^{-1}, respectively. The antibacterial activity of AP@58S-2 was significantly enhanced compared with 58S-2 alone ($p < 0.05$). Complementary agar well diffusion assays were performed at the MIC to visualize direct antibacterial activity (Fig. 7B). Clear inhibition zones were observed for all tested samples, with AP@58S-2 displaying a distinct growth suppression halo comparable to or larger than those of the AP extract and 58S-2 alone. No MBC was observed for 58S-2 within the tested concentration range. In contrast, both the AP extract and AP@58S-2 demonstrated bactericidal activity, with MBC values of 0.75 mg mL^{-1} and 2.0 mg mL^{-1}, respectively. The calculated MBC/MIC ratios were 3.0 for the AP extract and 1.33 for AP@58S-2. An MBC/MIC ratio ≤ 4 is widely accepted as indicative of bactericidal activity, whereas higher values suggest bacteriostatic behavior. Accordingly, AP@58S-2 can be classified as bactericidal, while pristine 58S-2 exhibits only bacteriostatic effects. To further substantiate the antibacterial efficacy of AP@58S-2, its effect on biofilm-associated bacterial viability was evaluated by quantifying colony-forming units (CFUs), as shown in Fig. 7C. Two-way ANOVA revealed that both exposure time and type of antimicrobial agent had statistically significant effects on biofilm CFUs ($p < 0.01$), while no significant interaction between these two factors was observed ($p > 0.05$). No statistically significant differences in CFU counts were detected between the treated groups and the control during the initial 6 h of exposure ($p > 0.05$). In contrast, significant reductions in CFUs were observed at 12 h and 24 h for the treated groups compared with the control (all $p < 0.01$), indicating a time-dependent antibiofilm effect of AP@58S-2. The performance of the composite compared favorably to its individual components, suggesting a synergistic effect between the bioactive glass matrix and the phytochemical-rich AP extract. The mechanism is likely multifactorial, involving both ionic dissolution products (*e.g.*, Ca^{2+}, SiO_4^{4-}) that can destabilize bacterial cell walls and bioactive molecules from the AP extract that may interfere with bacterial metabolism and quorum sensing. This outcome supports the notion that the composite retains the bactericidal or bacteriostatic properties of its constituents while potentially enhancing efficacy through combined mechanisms. In the context of clinical application, the ability to suppress *S. mutans* colonization could reduce the risk of post-implant infection and biofilm-related complications.

Taken together, the results presented highlight the multifunctional bioactivity of AP@58S-2. The composite not only supports hMSC survival without inducing acute cytotoxic effects but also provides robust antioxidant activity, particularly against ABTS, DPPH radicals, which could help attenuate oxidative stress *in vivo*. Furthermore, the antibacterial data demonstrate the ability of AP@58S-2 to inhibit the growth of *S. mutans* through both growth suppression in liquid culture and direct inhibition on solid media. The convergence of these properties—cytocompatibility, antioxidant capacity, and antibacterial activity—positions AP@58S-2 as a promising biomaterial for regenerative medicine applications, especially in environments where infection control and oxidative stress management are critical.[14] In scenarios such as oral bone regeneration, periodontal therapy, or implant coatings, these attributes could synergistically improve healing outcomes by simultaneously promoting tissue integration, reducing inflammation, and preventing microbial colonization. The integration of plant-derived bioactive into the bioactive glass matrix represents a strategic approach to designing multifunctional biomaterials capable of addressing multiple clinical challenges within a single platform.

3.7 Benchmarking advances in bioactive glass in combination with plant extract for dental application

To contextualize the present study, a benchmarking comparison of bioactive glasses combined with plant-derived extracts for biological applications over the last 5–10 years is presented in Table 2. Previous studies[23–25,28–33] consistently demonstrate that the incorporation of herbal extracts into bioactive glass matrices enhances biological performance beyond that of pristine bioactive glass. While bioactive glasses inherently exhibit bioactivity and limited antibacterial effects due to ionic dissolution and local pH elevation,[6] their standalone antibacterial efficacy is often weak and highly dependent on glass composition and the specific oral bacterial strain involved.[23,24,29,32] In many reported cases,[23–25,30] inhibition zone diameters fall below the antibacterial activity threshold defined by standard guidelines (*e.g.*, SNV 195920-1992), and indicating insufficient antimicrobial potency when bioactive glass is used alone.

Importantly, Table 2 highlights a clear research trend toward integrating phytotherapeutics with engineered bioactive glasses to overcome these limitations and introduce additional biological functions relevant to dental applications. Herbal extracts are rich in phenolics, flavonoids, terpenoids, and other bioactive compounds that provide direct antibacterial activity[1,19] and contribute antioxidant and anti-inflammatory effects that are not intrinsic to bioactive glass. This multifunctionality is particularly relevant for tissue regeneration applications, including particularly important in dental care, including restorative materials, implant coatings, periodontal therapies,

Table 2 Benchmarking of bioactive glasses loaded with plant extracts for biological applications

Bioactive glass composition	Plant extract	Main phytochemicals	Loading efficacy/efficiency[a]	Biological performance of BG alone	Performance after plant loading	Application	Ref.
Mesoporous BG (58 wt% SiO_2, 37 wt% CaO, 5 wt% P_2O_5)	*Boswellia sacra* extract	Boswellic acids	1.98% (9.9 ± 0.1 mg per 500 mg BG)	No antibacterial activity	Enhanced antibacterial and mineralization ability	Bone regeneration	27
Mesoporous BG ($70SiO_2$–30CaO in mol%)	*Peganum Harmala*	Alkaloids (harmine, harmaline)	n/a	Weak antibacterial activity	Significantly enhanced antibacterial activity	Bone tissue engineering	32
BG ($40SiO_2$–54CaO–$6P_2O_5$ in mol%)	*Salvia officinalis* L.	Phenolics, flavonoids	1.5, 3, and 4.5% w/w	No radical scavenging; stimulated intracellular ROS; promoted osteoblast differentiation	Strong radical scavenging; reduced intracellular ROS; enhanced antibiofilm activity; improved hydrophilicity and apatite formation	Bone tissue engineering	31
Bioglass® 45S5	*Cinnamomum cassia*	Phenolics, flavonoids	$16 \pm 10\%$	No antioxidant activity, weak antibacterial activity, poor antibiofilm effect	Improved antioxidant and antibacterial, showing a significant improvement in anti-biofilm activity	Bone tissue engineering	30
Mesoporous BG	*Origanum vulgare*	Phenolics, flavonoids	~4.45 mg extract per g BG	No antibacterial effect	Slowed bacterial growth	Bone tissue engineering	25
Mesoporous BG ($70SiO_2$–30CaO in mol%)	*Syzygium aromaticum*	Eugenol	5.8 ± 0.1 μg per mg BG	Weak antibacterial; no antioxidant activity	Improved antibacterial (*E. coli*, *S. aureus*) and antioxidant activity	Bone infections and oxidative stress	29
Mesoporous BG (60% SiO_2, 30% CaO, 10% P_2O_5 in mol)	*Melaleuca armillaris*	Terpenoids	~38.4 μL per g BG	Weak antibacterial activity	Enhanced antibacterial properties	Coatings and tissue engineering scaffolds	24
Bioglass® 45S5	*Cissus quadrangularis*	Flavonoids, phenolics	n/a	Weak antioxidant activity	Improved antioxidant activity and biocompatibility	Regenerative applications	28
Bioglass ($SiO_2/Na_2O = 1$ by mol)	*Nigella sativa* L.	Thymoquinone	1.5 and 3 wt%	No antimicrobial activity	Efficient antimicrobial performance	Bone healing	23
58S BG	*Andrographis paniculata*	Andrographolide, phenolics	~65% loading (~10.6 μg mg^{-1} BG)	Bioactive, bacteriostatic	Bactericidal (MBC/MIC = 1.33), antioxidant, cytocompatible	Dental regeneration	This work

[a] Loading amounts are reported as described in the original references. "n/a" indicates that no information was available.

and bone substitute materials, where biomaterials inevitably elicit a foreign body response, including inflammation and the generation of reactive oxygen species (ROS).[34] While an acute inflammatory response can support angiogenesis and tissue repair, excessive or prolonged ROS production can impair osseointegration, delay periodontal healing, and increase the risk of implant failure.[35]

The incorporation of herbal extracts into bioactive glass matrices has been shown to mitigate these adverse effects by introducing antioxidant activity capable of scavenging ROS and modulating inflammatory pathways.[27,34] As summarized in Table 2, several plant-loaded bioactive glass systems exhibit enhanced radical scavenging activity (*e.g.*, DPPH, ABTS), improved cytocompatibility, and reduced oxidative stress, in addition to strengthened antibacterial performance.[24,29,30,32] Moreover, the dissolution behavior of the glass network enables controlled and sustained release of phytochemicals, ensuring localized biological activity while minimizing systemic exposure.[23,28,31] This controlled release mechanism allows the antibacterial and antioxidant effects of herbal compounds to act synergistically with the pH- and ion-mediated antibacterial properties of the glass.

In line with these observations, the present study demonstrates that loading *Andrographis paniculata* extract into morphology-controlled spherical 58S bioactive glass results in a multifunctional material that combines bactericidal activity, antibiofilm efficacy, antioxidant capacity, and excellent cytocompatibility. By simultaneously supporting mineralization, suppressing bacterial colonization, and alleviating oxidative stress, this integrated approach advances the current state of bioactive glass–plant extract composites and underscores their potential for regenerative applications, particularly in challenging environments such as the oral cavity.

4. Conclusion

In this study, a two-step sol–gel approach was used to prepare 58S bioactive glass with spherical morphology and well-defined textural properties. Compared with the one-step route, the two-step synthesis produced particles with higher surface area and more uniform porosity, which contributed to moderated pH variations during immersion and improved cytocompatibility. The resulting 58S-2 glass provided a suitable porous matrix for the incorporation of *Andrographis paniculata* extract. The AP-loaded composite (AP@58S-2) exhibited efficient extract loading and a sustained release profile. *In vitro* evaluations showed that AP@58S-2 was well tolerated by human mesenchymal stem cells and exhibited antioxidant activity associated with the presence of phytochemicals from the plant extract. Antibacterial testing demonstrated enhanced inhibitory effects against *Streptococcus mutans* compared with unloaded bioactive glass, including bactericidal behavior as indicated by the MBC/MIC ratio and a time-dependent reduction in biofilm viability. Overall, the results indicate that combining morphology-controlled 58S bioactive glass with a plant-derived extract can provide simultaneous mineralization-related bioactivity, antibacterial effects, and antioxidant functionality. This study provides experimental evidence supporting the feasibility of using plant-extract-loaded bioactive glass as a multifunctional material for dental-related applications, where infection control and oxidative stress management are important alongside tissue regeneration.

Conflicts of interest

The authors declare that they have no known competing financial interests or personal relationships that could have appeared to influence the work reported in this paper.

Data availability

Data was included in the manuscript.

Acknowledgements

Author wants to thank Dr Tuan Tran (US-VNU) for the bacteria test and MSc Lam Nguyen (HUIT) for SEM measurement. This research is funded by Vietnam National University Ho Chi Minh City (VNU-HCM) under grant number C2023-44-03.

References

1 P. Pradeep, A. R. Thomas, K. Kaur, R. S. Samson, A. Mayya, S. Adiga and S. Kumbargere Nagraj, Herbal medicines to prevent dental caries, *Cochrane Database Syst. Rev.*, 2024, **5**(5), CD015832.
2 D. Khvostenko, T. J. Hilton, J. L. Ferracane, J. C. Mitchell and J. J. Kruzic, Bioactive glass fillers reduce bacterial penetration into marginal gaps for composite restorations, *Dent. Mater.*, 2016, **32**(1), 73–81.
3 F. Hasan, H. Setia Budi, R. Ramasamy, T. Tantiana, R. D. Ridwan, E. R. Winoto, P. Nuraini, J. Handajani, A. A. Djais and S. Anitasari, A systematic review of Streptococcus mutans and Veillonellae species interactions in dental caries progression: positive or negative impact?, *F1000Research*, 2024, **13**, 1080.
4 E. Piatti, M. Miola and E. Verne, Tailoring of bioactive glass and glass-ceramics properties for in vitro and in vivo response optimization: a review, *Biomater. Sci.*, 2024, **12**(18), 4546–4589.
5 F. Vietanti, T. A. Lee, H. Y. Tseng and Y. J. Chou, Investigation of in vitro bioactivity, and osteoblast and angiogenic activity of spray-dried boron-doped 58S bioactive glass microspheres, *RSC Adv.*, 2023, **13**(51), 36071–36078.
6 D. Zhang, O. Lepparanta, E. Munukka, H. Ylanen, M. K. Viljanen, E. Eerola, M. Hupa and L. Hupa, Antibacterial effects and dissolution behavior of six bioactive glasses, *J. Biomed. Mater. Res., Part A*, 2010, **93**(2), 475–483.
7 I. E. L. Viana, R. Borges, J. Marchi, S. Feitosa, M. M. Marques and T. Scaramucci, A 58S bioactive glass for dentin hypersensitivity and erosive tooth wear: an in vitro study, *J. Dent.*, 2022, **127**, 104343.

8 Y. J. Han, S. C. Loo, J. Lee and J. Ma, Investigation of the bioactivity and biocompatibility of different glass interfaces with hydroxyapatite, fluorohydroxyapatite and 58S bioactive glass, *Biofactors*, 2007, **30**(4), 205–216.
9 M. Borden, L. E. Westerlund, V. Lovric and W. Walsh, Controlling the bone regeneration properties of bioactive glass: effect of particle shape and size, *J. Biomed. Mater. Res., Part B*, 2022, **110**(4), 910–922.
10 T. A. Ostomel, Q. Shi, C. K. Tsung, H. Liang and G. D. Stucky, Spherical bioactive glass with enhanced rates of hydroxyapatite deposition and hemostatic activity, *Small*, 2006, **2**(11), 1261–1265.
11 W. Xie, X. Chen, Y. Li, G. Miao, G. Wang, T. Tian, L. Zeng and X. Che, Facile synthesis and in vitro bioactivity of radial mesoporous bioactive glass with high phosphorus and calcium content, *Adv. Powder Technol.*, 2020, **31**(8), 3307–3317.
12 B. Yu, C. A. Turdean-Ionescu, R. A. Martin, R. J. Newport, J. V. Hanna, M. E. Smith and J. R. Jones, Effect of calcium source on structure and properties of sol-gel derived bioactive glasses, *Langmuir*, 2012, **28**(50), 17465–17476.
13 S. Lin, C. Ionescu, K. J. Pike, M. E. Smith and J. R. Jones, Nanostructure evolution and calcium distribution in sol–gel derived bioactive glass, *J. Mater. Chem.*, 2008, **19**, 1276–1282.
14 M. A. S. Melo, I. M. Garcia, T. Alluhaidan, M. Qaw, C. Montoya, S. Orrego, A. A. Balhaddad and L. Mokeem, The next frontier in antibacterial dental resins: a 20-year journey of innovation and expectations, *Dent. Mater.*, 2025, **41**(9), 1045–1057.
15 B. Avula, K. Katragunta, K. K. Tatapudi, Y. H. Wang, Z. Ali, A. G. Chittiboyina and I. A. Khan, Phytochemical analysis of phenolics and diterpene lactones in Andrographis paniculata plant samples and dietary supplements, *J. Pharm. Biomed. Anal.*, 2025, **262**, 116866.
16 S. B. Naik, N. K. Kumar, P. A. Swathisha, B. Brigit, H. S. Preetham and C. S. Karumaran, Effect of Andrographis paniculata Herbal Extract on Cytotoxicity, Proliferation and Osteogenic/Odontogenic Differentiation of Human Dental Pulp Stem Cells: An In vitro Study, *Indian J. Dent. Res.*, 2024, **35**(2), 196–200.
17 J. Plianrungsi and P. Kulthanaamondhita, Comparison of Andrographis paniculata and Chlorhexidine Mouthwash on Anti-plaque, Anti-gingivitis and Side Effects, *J. Dent. Assoc. Thai.*, 2021, 321–333.
18 A. A. A. Muhamad, T. N. T. Kub, H. Miran, S. Mohamad, T. N. N. T. Ismail, M. E. Yusoff, R. Abdullah, S. I. T. I. Asma'hassan, Z. N. Salmuna and N. N. Ahmad, Evaluation of toxicity and antibacterial activities of Andrographis paniculata herbal mouthwash against oral pathogens, *Malays. Appl. Biol.*, 2022, **51**(3), 71–78.
19 P. T. N. Trinh, N. C. Truc, T. T. Danh, N. T. T. Trang, D. T. Le Hang, L. N. T. Vi, Q. T. Hung and L. T. Dung, A study on the antioxidant, anti-inflammatory, and xanthine oxidase inhibitory activity of the Artemisia vulgaris L. extract and its fractions, *J. Ethnopharmacol.*, 2024, **334**, 118519.
20 X. Kesse, C. Vichery and J.-M. Nedelec, Deeper Insights into a Bioactive Glass Nanoparticle Synthesis Protocol To Control Its Morphology, Dispersibility, and Composition, *ACS Omega*, 2019, **4**(3), 5768–5775.
21 Y. Cui, S. Hong, W. Jiang, X. Li, X. Zhou, X. He, J. Liu, K. Lin and L. Mao, Engineering mesoporous bioactive glasses for emerging stimuli-responsive drug delivery and theranostic applications, *Bioact. Mater.*, 2024, **34**, 436–462.
22 M. Mneimne, R. G. Hill, A. J. Bushby and D. S. Brauer, High phosphate content significantly increases apatite formation of fluoride-containing bioactive glasses, *Acta Biomater.*, 2011, **7**(4), 1827–1834.
23 S. Tiji, M. Lakrat, Y. Rokni, E. M. Mejdoubi, C. Hano, M. Addi, A. Asehraou and M. Mimouni, Characterization and Antimicrobial Activity of Nigella sativa Extracts Encapsulated in Hydroxyapatite Sodium Silicate Glass Composite, *Antibiotics*, 2022, **11**(2), 170.
24 J. Ballarre, D. Buldain, I. Unalan, J. I. Pastore, N. Mestorino and A. R. Boccaccini, Melaleuca armillaris Essential Oil as an Antibacterial Agent: The Use of Mesoporous Bioactive Glass Nanoparticles as Drug Carrier, *Nanomaterials*, 2022, **13**, 34.
25 Z. Najam, S. A. Batool, M. Abdullah, S. M. H. Gillani, K. Yaqoob, A. Niaz, A. Imran and M. A. U. Rehman, Natural antibiotic Oregano loaded mesoporous bioactive nanoparticles for bone tissue engineering applications: a detailed in-vitro analysis, *J. Drug Delivery Sci. Technol.*, 2026, **115**, 107642.
26 Y. K. Chung, C. Y. Hsu, Y. T. Wang, T. T. P. Tran, A. Alalaiwe and J. Y. Fang, Nanocarrier-enabled delivery of natural antiobesity agents, *Nanomedicine*, 2025, **20**(16), 2167–2187.
27 K. Ilyas, L. Singer, M. A. Akhtar, C. P. Bourauel and A. R. Boccaccini, Boswellia sacra Extract-Loaded Mesoporous Bioactive Glass Nano Particles: Synthesis and Biological Effects, *Pharmaceutics*, 2022, **14**(1), 126.
28 S. Chitra, S. Rajeshkumar, R. Ramya, P. Bargavi and S. Balakumar, Probing the biocompatibility and antioxidant properties of Cissus quadrangularis conjugated bioactive glass and hydroxyapatite towards regeneration application, *Inorg. Chem. Commun.*, 2023, **157**, 111398.
29 A. I. Damian-Buda, I. Unalan and A. R. Boccaccini, Combining Mesoporous Bioactive Glass Nanoparticles (MBGNs) with Essential Oils to Tackle Bacterial Infection and Oxidative Stress for Bone Regeneration Applications, *ACS Biomater. Sci. Eng.*, 2024, **10**(11), 6860–6873.
30 I. Unalan, T. Fuggerer, B. Slavik, A. Buettner and A. R. Boccaccini, Antibacterial and antioxidant activity of cinnamon essential oil-laden 45S5 bioactive glass/soy protein composite scaffolds for the treatment of bone infections and oxidative stress, *Mater. Sci. Eng., C*, 2021, **128**, 112320.
31 M. Dziadek, K. Dziadek, K. Checinska, B. Zagrajczuk, M. Golda-Cepa, M. Brzychczy-Wloch, E. Menaszek,

A. Kopec and K. Cholewa-Kowalska, PCL and PCL/bioactive glass biomaterials as carriers for biologically active polyphenolic compounds: comprehensive physicochemical and biological evaluation, *Bioact. Mater.*, 2021, **6**(6), 1811–1826.

32 M. Bibi, S. A. Batool, S. Iqbal, S. B. Zaidi, R. Hussain, M. Akhtar, A. Khan, M. S. Alqahtani, M. Abbas and M. A. Ur Rehman, Synthesis and characterization of mesoporous bioactive glass nanoparticles loaded with peganum harmala for bone tissue engineering, *Heliyon*, 2023, **9**(11), e21636.

33 K. Ilyas, L. Singer, M. A. Akhtar, C. P. Bourauel and A. R. Boccaccini, Boswellia sacra Extract-Loaded Mesoporous Bioactive Glass Nano Particles: Synthesis and Biological Effects, *Pharmaceutics*, 2022, **14**(1), 126.

34 K. Schuhladen, J. A. Roether and A. R. Boccaccini, Bioactive glasses meet phytotherapeutics: the potential of natural herbal medicines to extend the functionality of bioactive glasses, *Biomaterials*, 2019, **217**, 119288.

35 L. Singer and C. Bourauel, Herbalism and glass-based materials in dentistry: review of the current state of the art, *J. Mater. Sci. Mater. Med.*, 2023, **34**(11), 60.